Chapter 4

Magnetic-field-induced non-collinear to collinear spin transition in $NiBr_2$

4.1 Introduction

In this Chapter, presents the structural and magnetic properties of $NiBr_2$ along with other experimental results. To investigate the complex magnetic structure and microscopic features of phase transformation, extended magnetic measurements are conducted in the critical range of magnetic field (in-plane & out of plane direction) and temperature. The experimental results revealing the bulk magnetic measurement behaviors in terms of the helical spin structures as probed in the neutron diffraction experiment.

Here, $NiBr_2$ has been considered as a model system for a triangular spin-lattice that crystallizes in a hexagonal layer structure of the $CdCl_2$ type with a c-axis as a high symmetry axis. For a schematic of the crystal structure, see Fig. 3(a-c) in the Chapter 3. However, this section focuses on the study of the microscopic spin structure responsible for the observed field-induced incommensurate to commensurate spin transition in $NiBr_2$. For both magnetic phases, spins are arranged in a hexagonal plane that is orthogonal to the c-axis, which is an easy magnetization plane [131–133]. Further introduction of J_3, inter-plane interactions and magnetic anisotropy leads to the formation of more complex spin arrangements [131–133]. However, in the presence of various exchange interactions in multiferroic halides, not only the detailed insights of spin arrangements are lacking, but also the general relationship between spin arrangements and strength of applied magnetic

field on a triangular lattice largely remains elusive. Establishing these facts for the case of $NiBr_2$, which is a model system for halide multiferroics, is the primary objective of this work.

By employing the ac (dc)-magnetization and magnetic susceptibility, neutron diffraction, and small-angle neutron scattering (SANS), in this Chapter, this thesis work demonstrates various hidden properties of the incommensurate spiral phase in the triangular lattice of the helimagnets $NiBr_2$. The experimental findings suggest that $NiBr_2$ shows a helimagnetic ground state after the first-order transition upon reducing the temperature where an external moderate magnetic field induces rearrangement in helimagnetic spin textures, which well matched with previous observations [67, 68, 131–133]. Here, experimental results indicate a high-field-induced transition from incommensurate spiral phase to commensurate in a single crystal of $NiBr_2$. Neutron diffraction and small-angle scattering combined with high-field magnetization suggest that the magnetic phase transition above the first order metamagnetic transition at $H = 4$ T into a compensated commensurate antiferromagnetic structure. Both phenomena lead to a unique response of spin helix phase under external field (H) despite the similarity in the original crystal lattice, thereby indicating that even a slight difference in the magnetic interactions are critically reflected in the respective response in frustrated magnets.

The main objectives of this Chapter are three-fold: to experimentally probe the incommensurate spiral phase of $NiBr_2$ using SANS, combining this information with magnetic data from the same crystals, to decide whether the incommensurate spiral phase is responsible for any hidden physics. If so, determining whether these states are non-trivial forms and the second aim to combine various experimental techniques on this point. The Chapter is organized as follows. In the next section, crystal growth and experimental protocols used for neutron diffraction and SANS are described. The results and discussion part of the Chapter deal first with the crystal structure, then dc (ac)-magnetization and susceptibility, and neutron scattering measurements of $NiBr_2$. By measuring the variation in magnetization with the temperature of this critical field, the phase diagram of $NiBr_2$ in the H-T plane has been outlined. The Chapter closes by bringing together the conclusions of the study as a whole to find the answers of few critical questions like what are the driving forces behinds antiferro-helimagnetic transitions? What is the microscopic origin of the incommensurate propagation wave vector? However, this Chapter focuses on the study of the microscopic origin of incommensurate to commensurate phase transition in $NiBr_2$.

4.2 Experimental details

High-quality single crystals were prepared by the self-flux method as detailed in Chapter 3. Magnetic measurements were carried out in a Quantum Design PPMS up to a high value of the field of 14 T, applied in-plane and out of the plane direction. Magnetic hysteresis measurements were also carried out using the MPMS at various temperatures in magnetic fields up to $\pm$14 T with the field applied in and the out-of-plane direction. The low-temperature magnetic bulk measurements between 2 and 300 K were performed using the MPMS 7T device and PPMS 14T (Quantum Design) systems. Measurements and analyses of the dc (ac)-susceptibility have been carried out on $NiBr_2$ single crystals.

Neutron diffraction experiments were performed on the normal-beam diffractometer E2 and E4 at the BER II reactor of the Helmholtz-Zentrum Berlin, Germany [148]. To attained maximum scattering cross-section, a relatively larger crystal originating from the same badge has been used for neutron diffraction experiments. The sample (0.1 g) was fixed to an aluminum holder, and the magnetic field was applied along the vertical c-axis defining the horizontal *(h h l)* scattering plane. The accuracy of the alignment of the c-axis of the crystal along the magnetic field was approximately 0.5°. The shorter wavelength was utilized to reach the out of scattering plane incommensurate reflections. E2 and E4 instruments use pyrolytic graphite (002) monochromator for selecting the neutron wavelength λ = 2.4 Å [148]. To refine the magnetic structure of $NiBr_2$, data mainly collected in the *(h h l)* plane. Besides, the data also recorded in the *(h h 0)* plane.

The crystal and magnetic structure refinements were performed with the program Fullprof [149]. The nuclear scattering lengths b(Ni) = 1.03 fm, and b(Br) = 0.6795 fm were considered. For the absorption correction (Gaussian integration), study used the absorption coefficient $\mu = 0.12$ cm^{-1}. No secondary extinction correction has been applied. $\frac{\lambda}{2}$ filters used at both E2 and E4 instruments, which imply residual higher-order wavelength contamination at a level of less than 10^{-4}. The data were collected with two-dimensional position-sensitive ^{3}He-detectors that were of different sizes at respective instruments. Measuring the peak intensity while ramping the field/temperature performed the field and temperature-dependent scans. The integrated peak intensity was found by summing the counts in a small area of the detector surrounding the reflection. The small-angle neutron scattering measurements were carried out with instrument V4 at the BER II reactor. Magnetic fields up to 5 T have been applied step-wise along and perpendicular to the trigonal axis of the single-crystalline $NiBr_2$ using a horizontal-field cryomagnet that restricts the scattering geometry significantly. The V4, where experiments have also applied the magnetic field along the basal plane of the crystal, has been used in a configuration that covered 0.04 nm^{-1} < Q < 1.3 nm^{-1}.

4.3 Results and discussion

4.3.1 Magnetization and susceptibility

Fig. 4.1(a) illustrates the temperature dependence of the magnetic susceptibility $\chi = M/H$ of $NiBr_2$, where the M is the magnetization, and the H is the magnetic field between 1 and 14 T applied perpendicular to the c-axis. It is evident that $\chi(T)$ is field independent of temperatures above 80 K. At low temperatures, two well-distinguished anomalies can be discerned, marking magnetic phase transitions. These anomalies associated with the magnetic phase transition temperatures, which are stabilized according to expression (2)-

$$T_{N,m} = \frac{\partial T.\chi(T)}{\partial T} \tag{4.1}$$

In the presence of magnetic field, the upper transition between the paramagnetic state and an antiferromagnetic is detected across T_N = 44.6 (1) K, and the lower transition between AF and noncollinear magnetic order is marked at T_m = 21.8 (1) K. Obviously, both anomalies shift with the increasing field at the lower temperatures. The lower anomaly disappears for fields above 4 T. However, closer inspection reveals that the upper at T_N initially increases in temperature before it decreases again.

The inverse susceptibility shows Curie-Weiss behavior for $T > 70$ K as shown in the inset Fig. 4.1(a & b) represent the temperature dependence of $\chi(T)$ and its fit by a modified Curie-Weiss law according to formula as shown in Eq. (3)-

$$\chi = C/(T - \theta_p) + \chi_0 \tag{4.2}$$

where C represents the Curie constant and θ_p is the paramagnetic Curie temperature. This formula also involves the temperature-independent term χ_0. The best fit of data in 1 T above 150 K using this formula leads to the effective moment of μ_{eff} = 2.76 (1) μ_B being close to the effective moment expected for the S = 1, $3d^8$ electron configuration of Ni ions ($\sqrt{8} = 2.83$). The effective moment determined from data taken at 14 T amounts to 2.66 (1)μ_B. The best fit at 14 T is conferred in the inset of Fig. 4.1(a). The θ_p = 22.2 (1) K (at 1 T) and 28.1 (1) K at 14 T. Fig. 4.1(b) shows the temperature dependence of magnetic susceptibility measured for the various field with field applied along the c-axis. For this field orientation, magnetic susceptibility at high temperatures is field independent with anomalies visible at lower temperatures. The effective moment and the paramagnetic Curie temperature parameters are very similar to the other orientation (μ_{eff} = 2.74 (1) μ_B

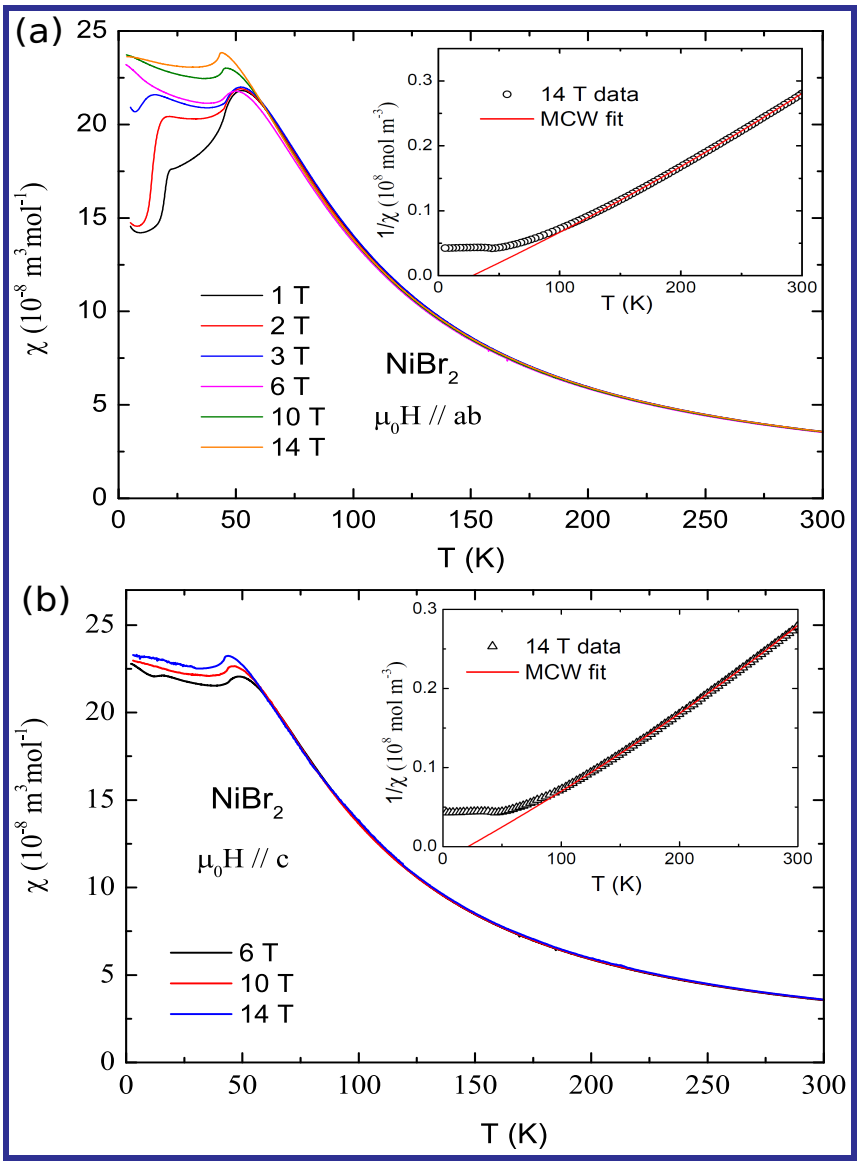

Fig. 4.1 (Color online)(a) Temperature dependence of $NiBr_2$ magnetic susceptibility measured with field applied parallel to (a-b) basal plane. The inset shows the temperature dependence of the inverse magnetic susceptibility $1/\chi(T)$ measured at 14 T is shown. (b) Temperature dependence of $NiBr_2$ magnetic susceptibility measured with field applied along the c-axis. The inset shows the temperature dependence of the inverse magnetic susceptibility $1/\chi(T)$ measured at 14 T is shown.

and θ_p = 21.3 (1) K, respectively). The best fit to data taken at 14 T applied along the c-axis is shown in the inset of Fig. 4.1(b).

The similarity between the magnetic susceptibility data with field-applied along and perpendicular to the c-axis suggests that the anisotropy of the paramagnetic state of $NiBr_2$ is negligible. However, this does not hold true for the state below T_N as magnetization (M-

H) curves taken for field applied perpendicular and along the c-axis are entirely different magnetization behavior, as depicted and compared in Fig. 4.2(a, b). Selectively, for the field applied within the basal (a-b) plane, a clear field-induced transition that shifts with increasing temperature to lower fields is evident. At 3 K, the magnetization step associated with the transition amounts to about 0.036 μ_B/Ni. The slope of the magnetization above the transition is higher than the lower temperatures. This is in good agreement with the magnetic susceptibility data. For the second scenario, when field applied along the c-axis there is no such transition that was evident.

In this subsection, an attempt was made to get a deeper insight into phase transitions in $NiBr_2$ through measuring the temperature and magnetic field dependence of ac-magnetic susceptibility, which is a complex value and reads $\chi_{ac} = \chi' - i\chi''$ where the real component χ', related to the reversible magnetization process, stays in-phase with the oscillating field, however, imaginary component χ'' is related to losses due to the irreversible magnetization process. These measurements would enable to distinguish para-(anti), and helimagnets and use of a static field H_{dc} would be helpful in determining the type of magnetic ordering across both phase transitions.

The ac susceptibility measurements were carried out as a function of temperature at different applied magnetic fields. To minimize the demagnetization effects, the dc magnetic field was applied within the basal plane (a–b). Fig. 4.3(a), illustrates the temperature dependence curves of the ac susceptibility measured in the vicinity of magnetic transitions (below 70 K). The results over the field range of 0.1 to 2.0 T show the maxima near phase transition. Over Tm, at low field strengths, the maxima shift towards a higher temperature [68].

Fig. 4.3(b) shows the χ' versus μ_0H curves at different temperatures in the range of 5-80 K. At T = 80 K, the χ' exhibits a nearly field independent curve. At T = 25 K, a peak can be noticed close to the upper phase boundary of the antiferromagnetic state as shown in the Fig. 4.1(a). Below T_m, a hysteretic nature of $\chi'_{H,T}$ curves is observed, confirming the signature of the helix nature of noncollinear spins. The shift in peak position with the magnetic field corresponds to the difference in torque required to reverse the helical spins by the applied magnetic field. These results indicate the transition from an incommensurate to a commensurate phase. The peak positions in $\chi'_{H,T}$ over the wide ranges map directly onto the field-induced modulation of the incommensurate phase. It should be noted that in the zero field, χ' diminishes monotonically in the temperature range of 5–20 K.

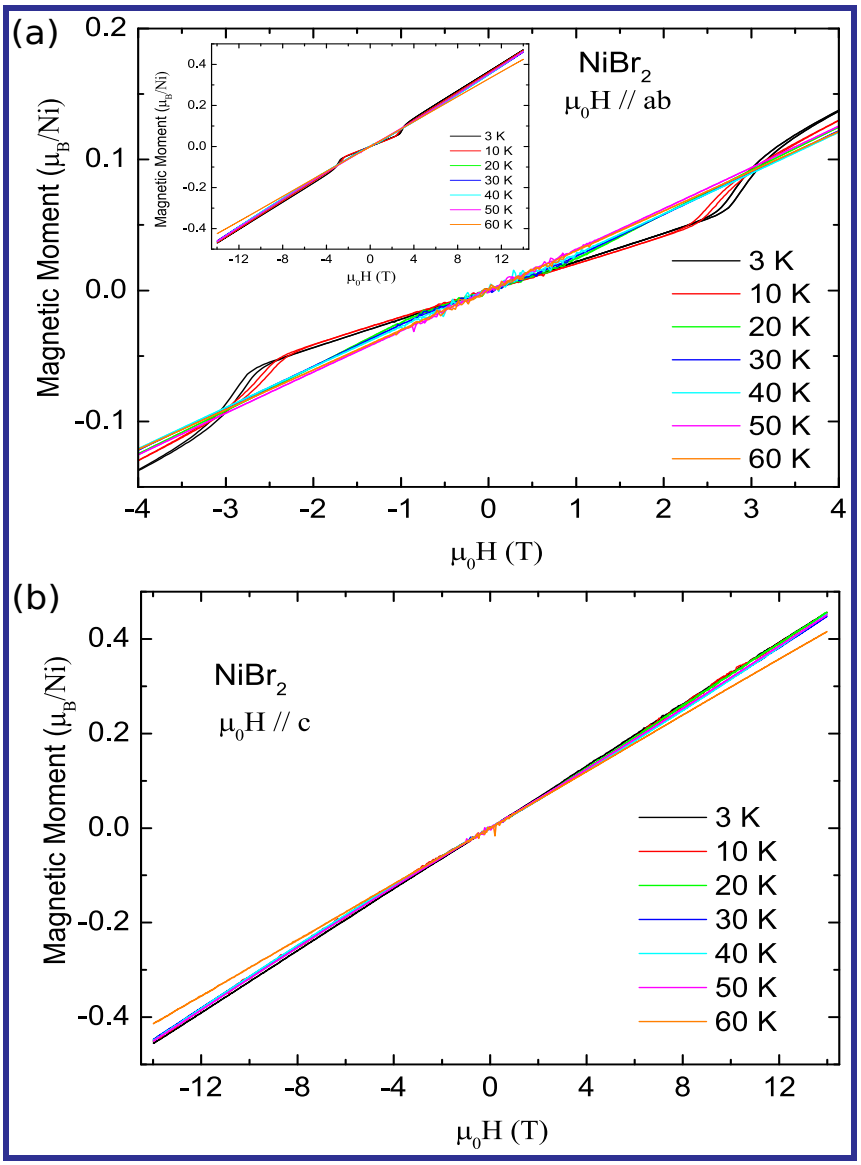

Fig. 4.2 (a) Field dependence of the $NiBr_2$ magnetization applied perpendicular to the c-axis at several different temperatures between 3 K and 60 K. The full field range between -14 T and +14 T is shown in the inset. (b) Field dependence of the $NiBr_2$ magnetization applied along the c axis at several different temperatures between 3 K and 60 K.

4.3.2 Neutron diffraction on $NiBr_2$

The crystal structure of $NiBr_2$ was determined using neutron diffraction data and Fullprof techniques [18,19]. $NiBr_2$ crystallizes in the $CdCl_2$ structure, which has the rhombohedral space group D^5_{3d} in the trigonal space group $R\bar{3}m$ [64, 67, 68, 131, 133]. In this space group, the Ni and Br atoms are situated at the Wyckoff positions 3a(0, 0, 0) and 6c(0, 0, z) with 3m and -3m local symmetries, respectively [131, 133].

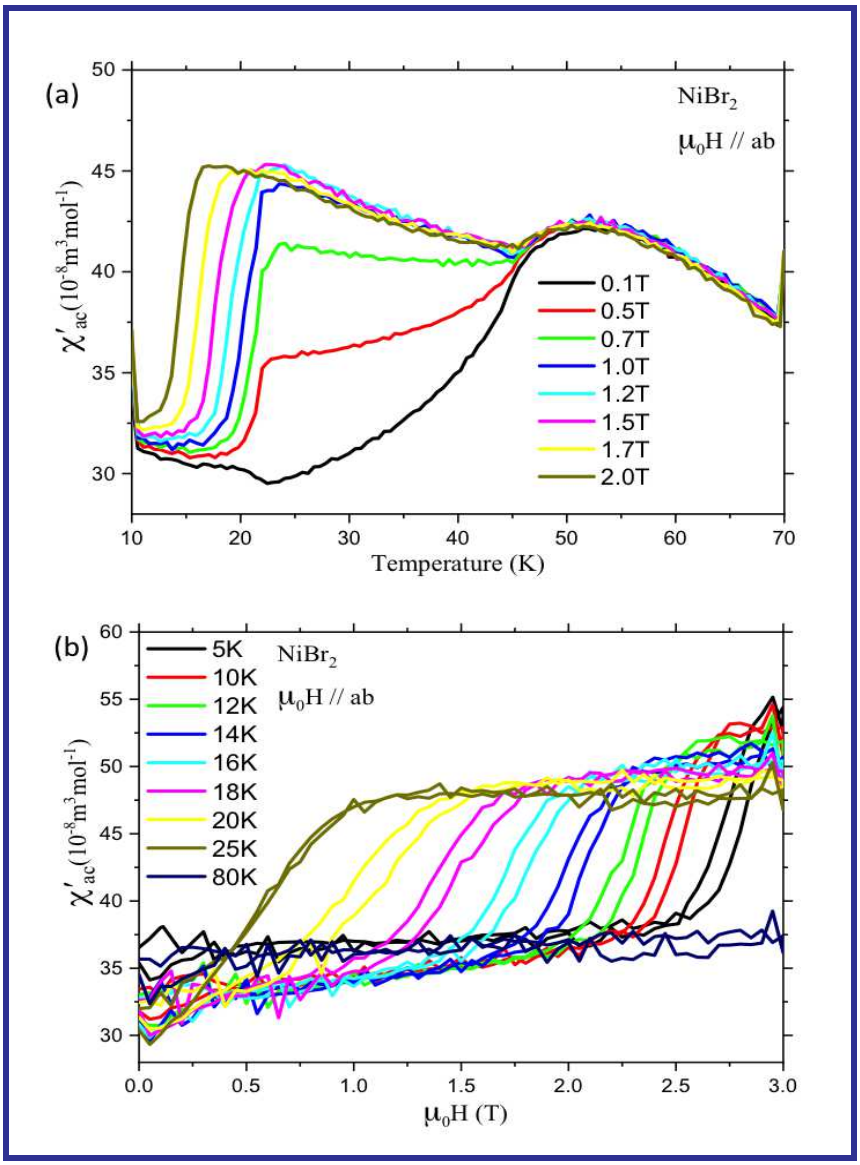

Fig. 4.3 (a) The temperature dependence of the ac susceptibility, $\chi_{H,T}$, of $NiBr_2$ in the vicinity of the lower transition(s), near 50 K, measured in various static applied fields between 0.1 and 2.5 T. Isothermal ac susceptibility $\chi_{H,T}$ measured over the range $25K \leq T \leq 80K$, $0.0 \leq H \leq 3.0T$ (b) The hysteresis regime corresponds to the incommensurate phase, $5K \leq T \leq 25K$. For higher temperature $25K \leq T \leq 80K$, $\chi_{H,T}$ shows a straight line confirming the compensated antiferromagnetic phase area.

Fig. 4.4(a) shows the (hhl) diffraction pattern recorded at 50 K. As it is evident that only (110), (003), (006), and (009) Bragg reflections are observed (along with signal originating from the Aluminum sample holder/cryostat). There are no unexpected Bragg reflections. The refinement of observed Bragg reflections leads to a reasonable agreement with literature data with the only structural free parameter zBr = 0.268 (8). As the

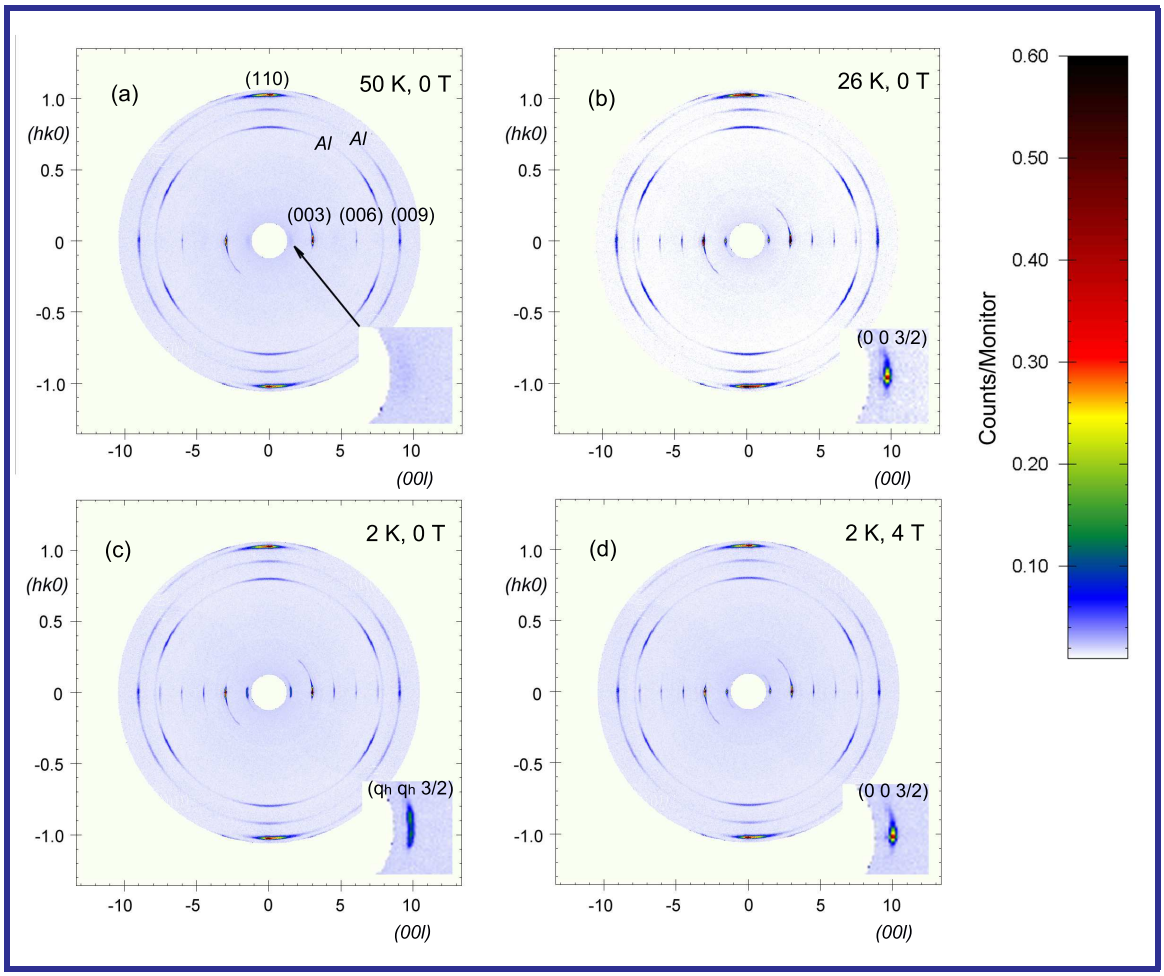

Fig. 4.4 Diffraction patters of the $NiBr_2$ single crystal as recorded using the E2 instrument in the (hhl) plane at mentioned conditions: (a) 50 K, 0 T, (b) 26 K, 0 T, (c) 2 K, 0 T and (d) 2 K, 4 T applied parallel of basal plan. In the insets the enlarged position around the (0 0 3/2) reciprocal space position is shown.

temperature is decreased below T_N (but above T_m), new Bragg reflections associated with AF order are observed. These can be indexed with a propagation vector q_c = (0 0 3/2) as shown in Fig. 4.4(b) and which is in well in agreement with literature. The pattern recorded at 26 K is shown. (0 0 3/2), (0 0 6/2) and (0 0 9/2) magnetic reflections show non-zero intensity. These magnetic satellite structures around the (003), (006), and (009) indicating antiferromagnetic ordering of Ni spins in the (a-b) basal plane. The Ni-spins forming planes perpendicular to the body diagonal are ferromagnetically aligned, whereas the spins in the neighboring planes are antiparallel [131, 133, 148].

As the incommensurate component's value at lower temperatures is expected to be very small, special care has been paid to improve the resolution of the diffractometer. In

the experiment, the wavelength (λ = 2.4 Å) of neutron reflected by a pyrolytic graphite monochromator, horizontal slits, is utilized to decrease the vertical divergence and graphite filters to remove the $\lambda/2$ contamination. These scans show that the component of the propagation vector along the c-axis remains commensurate with a value k_z value 3/2. However, an incommensurate component exists in the basal plane and is oriented along a $< 110 >$ direction. From 4.2 K to 22.8 K the propagation, vector has been found to be temperature-dependent. The k_z component remains commensurate to a value of 3/2. The in-plane component is always along a $< 110 >$ direction. An incommensurate component exists in the basal plane and is oriented along a $< 110 >$ direction. The absence of any second, third, or higher harmonics (see Fig. 4.4(c)) proves that $NiBr_2$ orders with a helical structure within the basal plane in zero fields at T = 4.2 K. The planes remain coupled antiferromagnetically. The magnetic satellites regain their shape similar to commensurate antiferromagnetic phase upon applying an in-plane magnetic field (H = 4 T) as shown in Fig. 4.4(d). This re-entrant behavior of magnetic satellite peak is reported for the first time in an incommensurate spin system in $NiBr_2$.

As the temperature is decreased below T_N (but above T_m), new Bragg reflections associated with AF order are observed. These can be indexed with a propagation vector q_c = (0 0 3/2) as shown in Fig. 4.4(b) and is well in agreement with literature. The pattern recorded at 26 K is shown. (0 0 3/2), (0 0 9/2) and (0 0 15/2) magnetic reflections show non-zero intensity.

Lowering the temperature further below T_m yields a change in the diffraction pattern. The q_c Bragg reflections split, as depicted in Fig. 4.4(c). The estimated propagation is of the $q_i = (q_h\ q_h\ 3/2)$, with q_h 0.03. There are no other magnetic reflections described by q_2 that are visible at 2 K, zero fields. These scans show that the propagation vector's component along the c-axis remains commensurate with a value k_z value 3/2. However, an incommensurate component exists in the basal plane and is oriented along a $< 110 >$ direction. From 4.2 K to 22.8 K, the propagation, vector has been found to be temperature-dependent. The k_z component remains commensurate to a value of 3/2. The in-plane component is always along a $< 110 >$ direction. An incommensurate component exists in the (a-b) basal plane and is oriented along a $< 110 >$ direction. The absence of any second, third, or higher harmonics (See Fig. 4.4(c)), proves that $NiBr_2$ orders with a helical structure within the basal plane in zero fields at T = 4.2 K. The planes remain coupled antiferromagnetically. Magnetic measurements have indicated for field applied within the (a-b) plane a magnetic phase transition around 3 T. Fig. 4.4(d) shows the pattern recorded at 2 K and 4 T. As can be seen, it is identical to the pattern recorded at 26 K (compare with Fig. 4.4(b). This can be at best seen from the insets of the relevant

panels. In the case of data taken at 50 K, one can also see a short-range order signal. Such field-induced spin reorientation in a single crystal of incommensurate $NiBr_2$ was observed with a magnetic field applied perpendicular to the c-axis. Spin reorientation occurred continuously with increasing field. At sample temperatures of 4.2 K and 22 K, complete reorientation was observed at critical fields of 4 T. The temperature dependence of the critical field is explained in terms of the interaction between Ni ions that can be further examined within the framework of spin-flop coupling.

4.3.3 Neutron scattering

Local lattice tilts on the sample surface can be caused by local lattice miss-orientations of crystallites, deformation strained grains, or due to grain boundaries, etc. In order to explore the quality of crystalline lattices, rocking curves of $NiBr_2$ crystal were recorded, which provides a way to explore small region of reciprocal space at a constant q-value with unprecedented the details of miss-orientation for different crystallites.

Fig. 4.5 shows the temperature dependence of the intensity of (0 0 3/2) reflection recorded with the zero magnetic field on cooling below 57 K. The solid line (red) represents the best fit of the experimental data satisfying the empirical relation through the points represents the best fit to expression (4.3)-

$$I(T) = b + I_0(1 - \frac{T}{T_N})^{2\beta} \tag{4.3}$$

where b is denoting the background intensity, I_0 represent the intensity at zero kelvin and the β is a critical parameter related to the dimensionality of the magnetic system. The best fit to this empirical formula that is valid in the critical region near the magnetic phase transition leads above 40K a good description of the data. The magnetic phase transition occurs at $T_N = 44.5\ (6)$ K with $\beta = 0.30\ (1)$. However, the observation of scattered intensity (see the non-negligible intensity above the background level in the Fig. 4.5 highlighted by the dashed line) above the T_N points to a presence of critical scattering in this material. The second order-order transition at T_m takes place at 21.6 (5) K. The non-zero intensity below T_m arises due to six new magnetic satellites, emerging in place of the original (0 0 3/2) Bragg reflection.

Fig. 4.6(a) shows the diffraction pattern recorded on E4 at 2 K at zero fields around the (0 0 3/2) reciprocal space position, using projection on the $\omega - \upsilon$ plane, where ω is the rotational angle of the sample and the υ is the deviation from the scattering plane [2θ]. As evident, the original magnetic Bragg reflection splits into six reflections indexed by three propagation vectors q_i = ($q_h q_h 3/2$), i = 1, 2, 3 (and associated opposite vectors). Using the

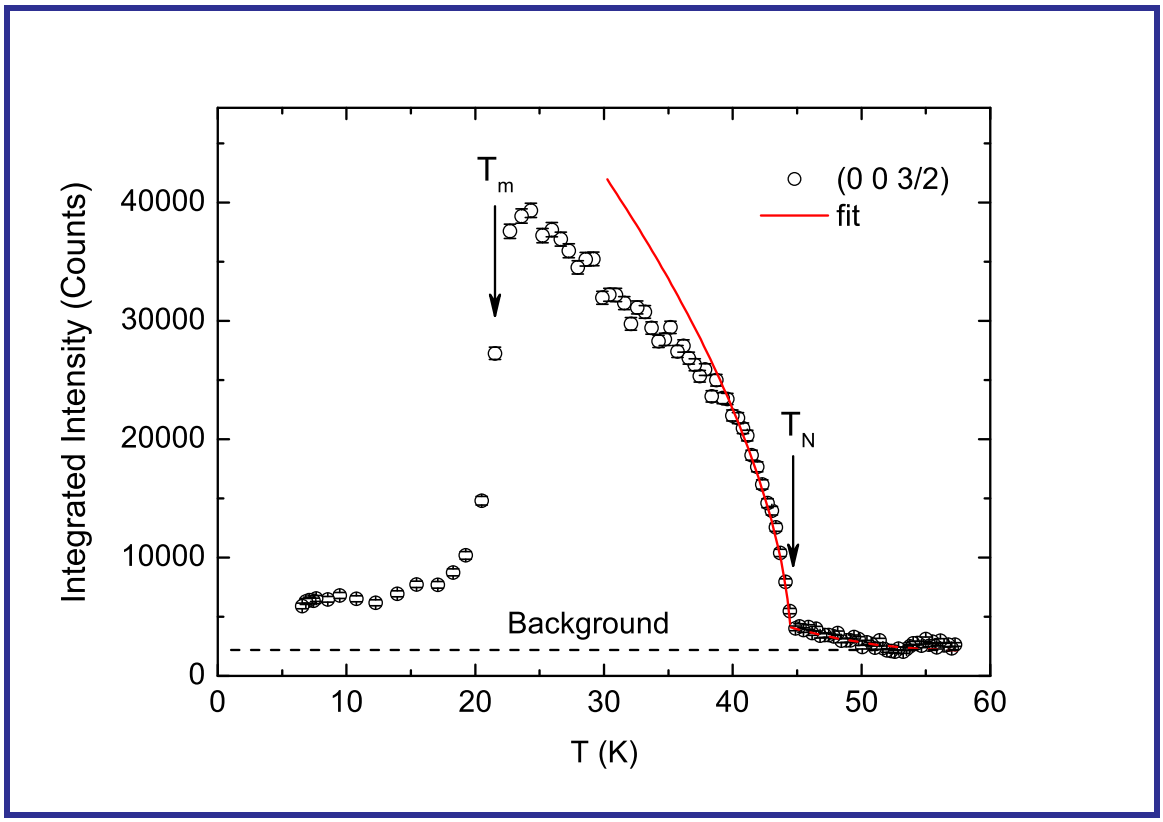

Fig. 4.5 The temperature dependence of the magnetic (0 0 3/2) Bragg reflection measured upon cooling at the top of the reflection. The solid-line through the points just below the T_N is the best fit to Eq. (4) given in the text. The transition at Tm takes place at 21.6 (5) K. Just above the T_N, a magnetic diffraction signal due to short-range correlations is visible. This is highlighted by a dashed line.

UB matrix refined from very few nuclear Bragg reflections and positions of the maxima it follows that q_h = 0.027 (1), which is in agreement with the literature [150]. The six magnetic reflections can be indexed as (-0.027 -0.027 3/2), (-0.054 0.027 3/2), (-0.027 0.054 3/2), (0.027 0.027 3/2), (0.054 -0.027 3/2) and (0.027 -0.054 3/2). These propagation vectors are incommensurate with the crystal structure. The projection of Fig. 4.6(a) on the rotational axis, ω is shown in Fig. 4.6(b), suggests that these six reflections have inhomogeneous intensities distribution. The existence of six magnetic propagation vectors at low temperatures raises the question whether one deals with a homogeneous state where the Ni magnetic moments are modulated in the whole volume of the sample by all the propagation vectors or whether one deals with spatially disjoint domains, each having one propagation vector. However, from the fact that, for instance, the reflection described by the propagation vector q_3 is by about 50 % more intense than the $-q_2$ reflection (see Fig.

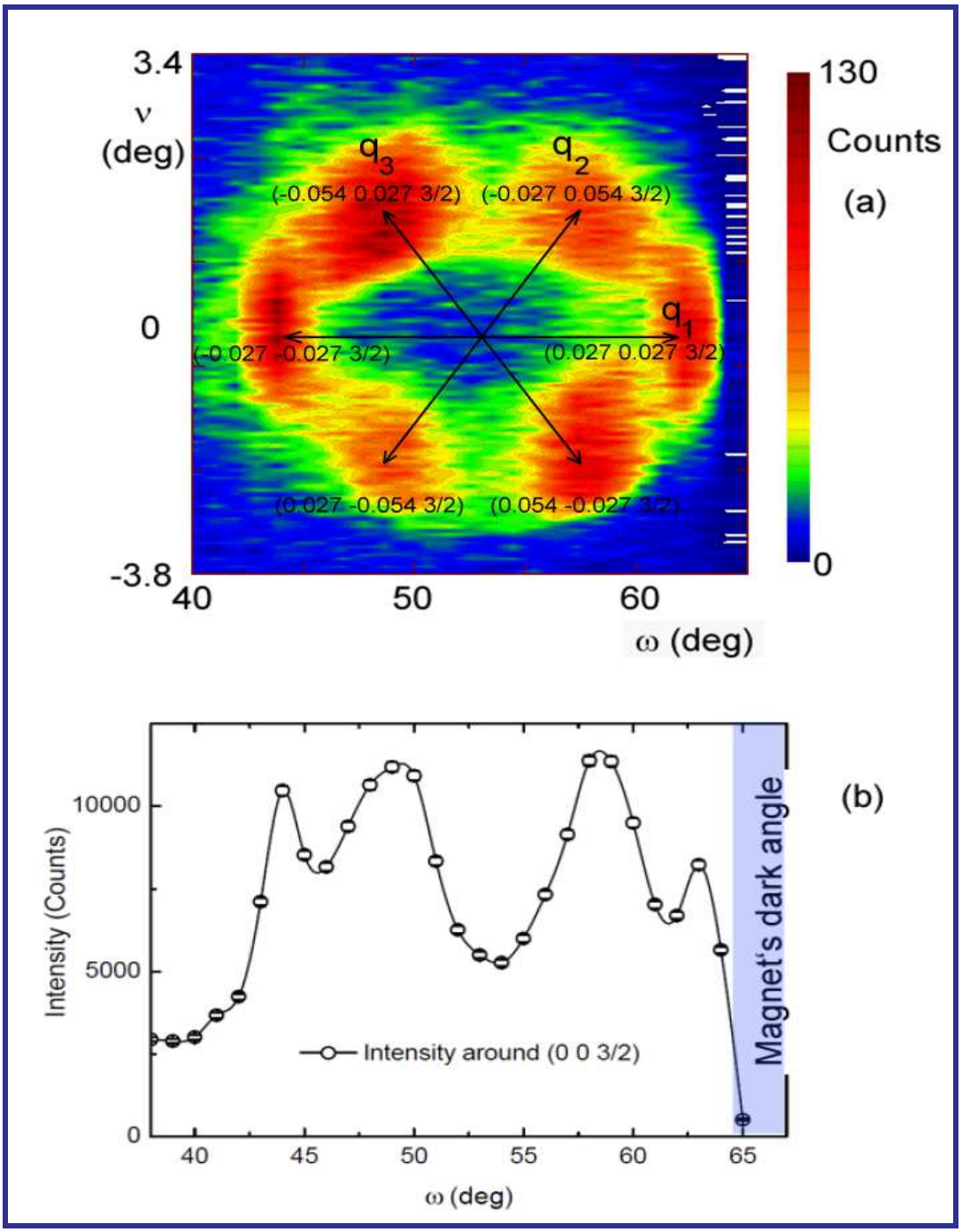

Fig. 4.6 (a) The diffraction pattern recorded with zero field around the (0 0 3/2) magnetic reflections in reciprocal space using $\omega - \upsilon$ projection (b) The conventional projection of diffraction pattern on the rotational $\omega-$ axis.

4.6 (a)), the former scenario can be ruled out. This confirms that the magnetic structure consists of volume-separated domains. From a symmetry viewpoint, the most distinctive

properties of the incommensurate spiral state from the 120° structures is that the ground state displays three-fold degeneracy, *i.e.*, three equivalent directions of wave vectors on the lattice. The ordered state is a single-q state with three equivalent wave vector directions. This three-fold degeneracy could also be a source of exotic ordered states, *e.g.,* various types of multiple-q states where multiple wave vectors coexist. The proper screw magnetic structure is realized at the magnetic ground state below T_N, where spins rotate within the plane perpendicular to the magnetic modulation vector. This means that the q-vector is slanted off from the triangular-lattice basal plane. Correspondingly, the spin-spiral plane is also canted from the plane, including the [001] axis.

Fig. 4.7(a) shows the temperature dependence of the diffracted intensities projected on the $\omega - axis$ along with projections on the $\omega - \upsilon$ plane (Fig. 4.7(b)) recorded at various temperatures. As can be seen, the six incommensurate reflections collapse at T_m to a single (0 0 3/2) reflection. Fig. 4.7(b) illustrates the temperature dependence of the intensity around the (0 0 3/2) position is shown. All the diffracted intensity is included, irrespective of whether originating from a commensurate or incommensurate magnetic state. The absence of any anomaly around T_m suggests that the (0 0 3/2) reflection just splits into the six reflections at a lower temperature without a significant change in the magnetic structure/magnetic moment magnitude. Symmetry analysis for both types of propagation vectors (commensurate and incommensurate) leads to the conclusion that Ni magnetic moments are oriented either along the c axis or perpendicular to it. In fact, the observed intensities observed intensities at (0 0 3/2) position suggests that the moments are not along the trigonal axis and are oriented within the plane. Due to the high symmetry of the crystal structure, it is not possible to determine the direction of these moments within the (a-b) basal plane.

The best fit of data collected under zero field at 25 K, leads to Ni moment magnitude of 2.8 (2) μ_B. This value is somewhat larger with respect to the literature data [131, 133]. The feasible magnetic structures are shown in Fig. 4.8. It should be stressed that this is one of several possible magnetic structures that agree equally with the data. The difference between the solution shown in Fig. 4.8(a, b) is that Ni moments are collinear in (Fig. 4.8 (a)) and smaller than in (see Fig. 4.8 (b)). The best fit to data taken at 2 K, 0 T as shown in Fig. 5.6 using six propagation vectors q_1 = (-0.027 -0.027 3/2), q_2 = (-0.054 0.027 3/2), q_3 = (-0.027 0.054 3/2), q_4 = (0.027 0.027 3/2), q_5 = (0.054 -0.027 3/2) and q_6 = (0.027 -0.054 3/2) leads to Ni magnetic moment of 3.0 (3) μ_B. The direction of Ni moments are changing within the basal plane in an incommensurate manner, making with respect to each other about α = 9.5 ° as one moves within the plane along a-axis as illustrated in Fig.

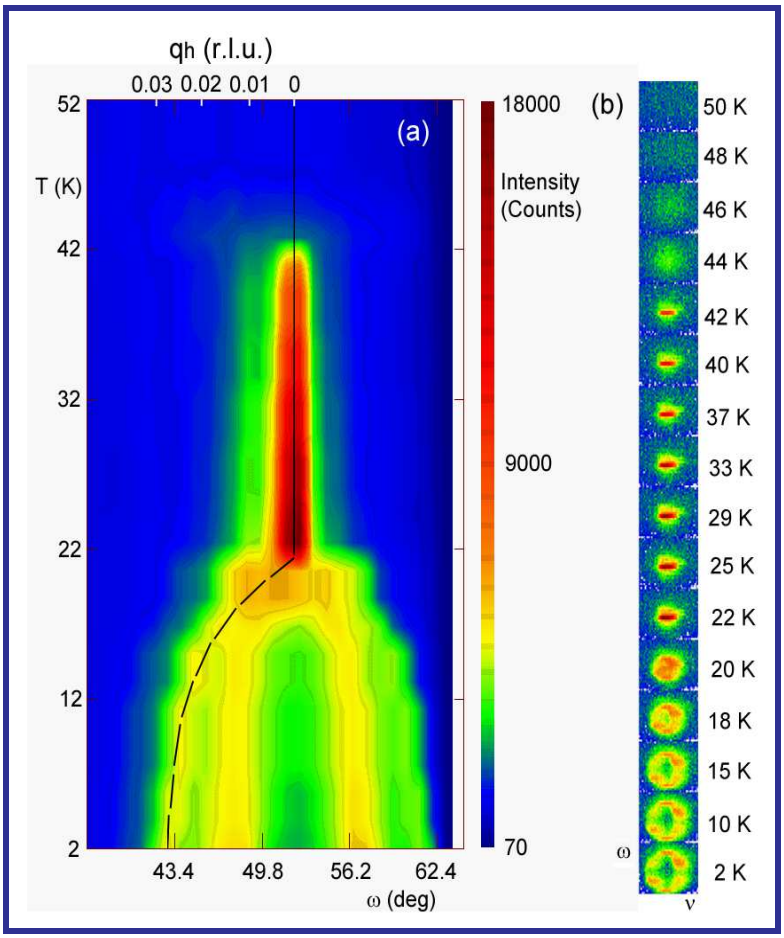

Fig. 4.7 (a) The temperature dependence of the diffracted signal around the magnetic (0 0 3/2) Bragg reflection projected on the ω-axis. The incommensurate component q_h is shown by the dashed line. It becomes zero above T_m. (b) Detected signal as seen on the 2D detector on E4 at various temperatures in the zero field.

4.8(c). This solution is in good agreement with literature data. The population of the six magnetic domains is about 18%: 10%: 22%: 13%: 19%: 18%.

This section, focuses on elaborating in more detail about the hidden observation of spin-flop tendency of the incommensurate spins that induced by a magnetic field (only above the critical value) applied within the (a-b) plane. The high-temperature magnetic phase is re-visited, which suggest only the magnetic reflections indexable with q_c = (0 0 3/2) are present. This is also documented in Fig. 4.9 (a), which shows the field dependence of the intensity projected on the omega-axis with increasing field. Merely the intensities of AF reflections are reduced with respect to the zero-field value, pointing to a smaller staggered magnetic moment of 2.5 (2) μ_B. No significant ferromagnetic component could

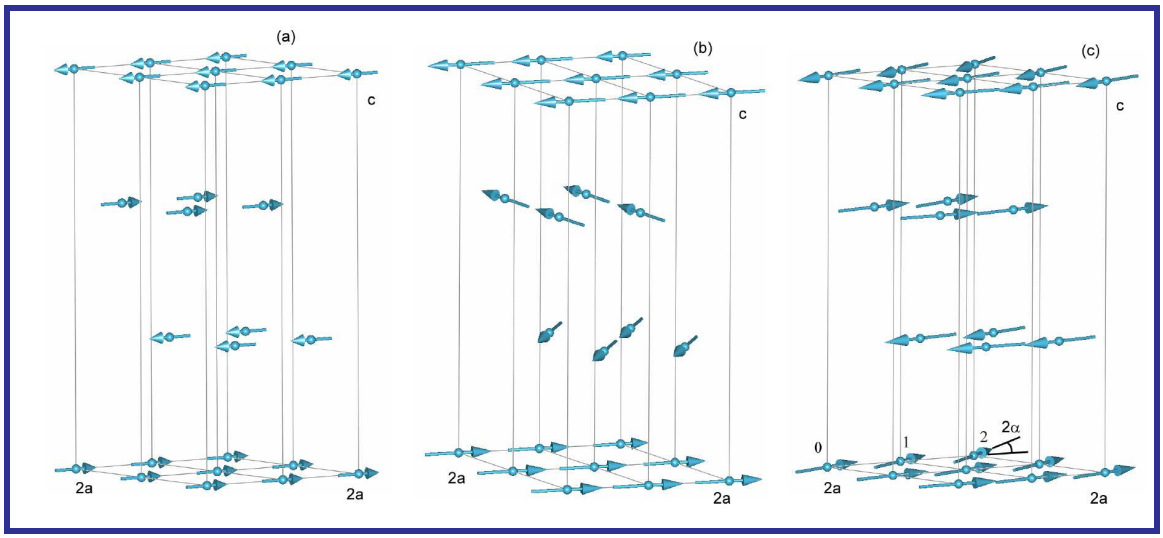

Fig. 4.8 Schematic representation of AF structure of $NiBr_2$ at 26 K, 0T (a) and 2 K , 0 T (c). A possible solution that agrees with data taken at 26 K, 0T equally well is shown in (b). Only Ni atoms are shown. In all cases $2 \times 2 \times 1$ crystallographic unit cells are shown. The moments in adjacent cell along the c axis are reverted.

be resolved. This is not surprising as the magnetization suggests a very small change in the magnetization connected with the transition.

In Fig. 4.9(a), the temperature dependence of the intensity around the (0 0 3/2) position measured with increasing temperature in a field of 2 T applied within the (a-b) plane. As can be seen, the lower transition shifts with respect to zero fields towards lower temperature while the upper transition stays approximately unchanged that in good agreement with magnetization data. As the field increases at 2 K above the critical field of about 3 T, only the magnetic reflections indexable with q_c = (0 0 3/2) are present. In Fig. 4.9(b) the temperature dependence of the intensity around (0 0 3/2) position measured with increasing temperature in a field of 5 T applied within the (a-b) plane is shown. Also, in this case, the T_N remains equal to approximately 44 K. This transition can be interpreted as in the presence of weak anisotropic energy, at a critical magnetic field the two sub-lattice magnetization rotates suddenly to a direction perpendicular to the easy magnetization direction, *i.e.*, c-axis, consequently perpendicular to the applied magnetic field, identical to spin-flop transition. Then a continuous rotation of the magnetic moment occurs upon increasing H.

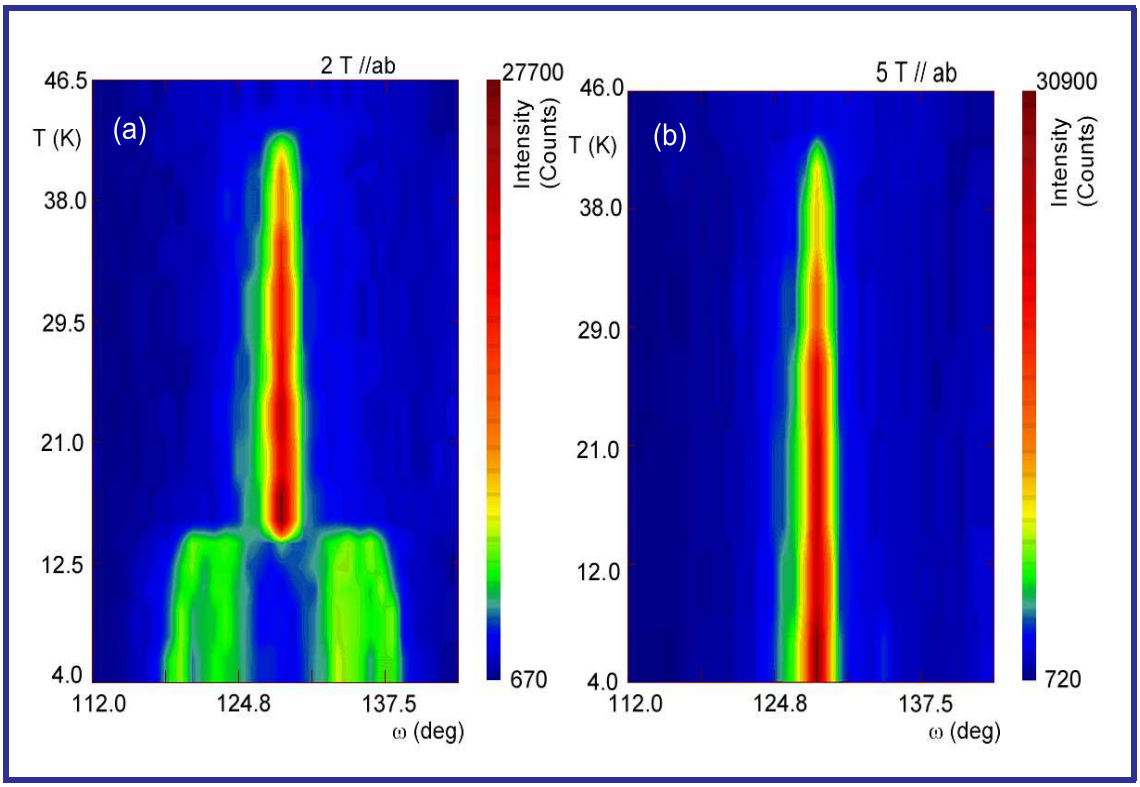

Fig. 4.9 (a) Field dependence of the intensity around the (0 0 3/2) in $\omega - \upsilon$ reciprocal plane and its projection on the $\omega-$ axis measured at 2 K with increasing field. (b) Temperature dependence of the intensity around the (003/2) measured with field of 2 T applied within the (a-b) plane. (c) Temperature dependence of the intensity around the (003/2) measured with field of 5 T applied within the (a-b) plane.

4.3.4 Phase diagram

In $NiBr_2$, the interaction that couples the magnetic moments are the exchange interactions, which have the long-range characteristic. Such exchange interactions may not only compete with each other, but they also interact with crystal field anisotropy. The interplay between these competing interactions may lead to incommensurate or amplitude-modulated magnetic structures where magnetic structures have periodicities that do not match the periodicity of the crystal lattice. The magnetic phase diagram of $NiBr_2$ near critical temperature T_m and T_N has been studied by simultaneous measurements of bulk magnetization and susceptibility as well as neutron small-angle scattering. It has been noticed that the new phases predicted by various approaches are existing across T_m and T_N upon cooling from a paramagnetic phase where the magnetic correlations exhibit a different characteristic and magnetic moment are randomly oriented. A sharp decrease of

the magnetic phase boundary at T_N results in a substantial increase of the satellite q-vector. As shown in the Fig. 4.10, for an intermediate temperature range in the (a-b) plane, a commensurate magnetic structure between 45K and 22 K was found by a least-squares refinement to be sinusoidally modulated with moments lying in the (a-b) plane. At lower temperatures and moderate magnetic field in the (a-b) plane, an incommensurate magnetic structure between 22 and 4 K was found by a least-squares refinement to be sinusoidally modulated with moments lying in the (a-b) plane, including an angle of $\gamma = 9.6^\circ$ with the basal plane. The magnetic phase diagram for an external field applied in the c-axis direction was also determined that confirms that upon reducing the temperature, one commensurate magnetic structure phase can evolve. The inset shows the extended field range that suggests for the field applied within the (a-b) plane yet another field-induced transition around 60 T.

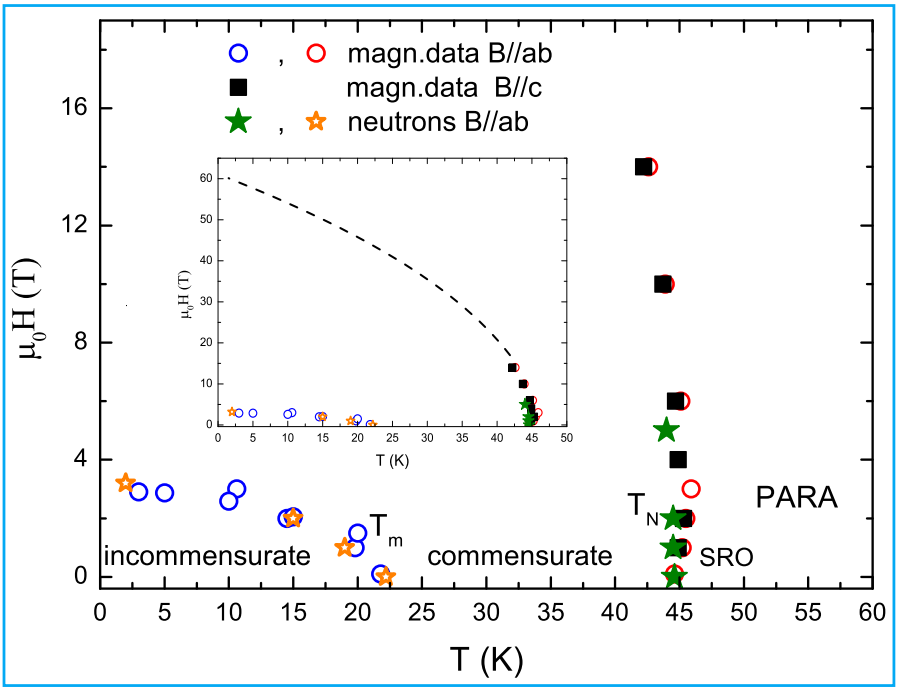

Fig. 4.10 Magnetic phase diagram of $NiBr_2$ constructed from magnetic bulk measurements (circles and squares) and neutron diffraction data (stars). In the inset a crude estimate of the critical field associated with the T_N is represented.

The behavior of $\chi_{H,T}$ may be a defining characteristic of such transitions, mainly reflecting the unusual combination of ferromagnetic and antiferromagnetic interactions in the $NiBr_2$ system, which leads to the complicated influence of applied fields on the spin configurations along the commensurate-incommensurate boundary. According to

Rastelli *et al.*, [26], when both J_{nn} and J_{nnn} are positive, the system behaves as ferromagnetic, but, when either or both are negative, helical or antiferromagnetic states are realized. A delicate balance of various exchange interactions prevails in a helical magnetic structure at lower temperatures, which enforces the system across the boundary from incommensurate-to-commensurate phase at elevated temperatures. The interplay between competing interactions leads to amplitude-modulated magnetic structure possesses a periodicity that is different from spatial distributions of spacing in the crystal [147, 151, 152].

4.4 Summary and conclusions

In conclusion, by measuring the magnetic properties and neutron diffraction of the triangular spin system of $NiBr_2$, the variation of the uniform exchange, the saturated magnetic moment, and the helical wave vector systematically vary with the change in the temperature and magnetic field were demonstrated. The changes measured in the magnetic properties are dominated by the variation of anisotropy and exchange interactions. These observations are supported by the models as predicted by Rastelli *et al.*, [26], after the simplified assumption of mutual competition in neighboring exchange interaction in triangular spin lattices. Despite this, across the incommensurate phase, demonstration of a new a new type of magnetic field induced phase transition reported. This hidden phase transitions entirely transform the low-temperature incommensurate phase into the high-temperature commensurate spin structure. This retention behavior of the incommensurate phase purely governs by the spin-flop transition. On the methodological side, this work demonstrates that combining state-of-the-art neutron scattering experiments with magnetization measurements allows extracting definitive microscopic information from the triangular spin system of $NiBr_2$, even when magnetic correlations are three-dimensional. These findings accelerate the search for exotic quantum states in helimagnetic systems through the screening of many related materials having direct technological implications. In conclusion, one may foresee that the accurate understanding of the role of the neighboring exchange interactions in the triangular spin systems paves the way to exploratory research on field-induced phase transitions where the choice of spin helices and topological magnetic texture will be a tool to improve the performances.